# Planar Sodium-Nickel Chloride Batteries with High Areal Capacity for Sustainable Energy Storage

*Tu Lan, Gustav Graeber, Louis Sieuw, Enea Svaluto-Ferro, Fabrizio Vagliani, Diego Basso, Alberto Turconi, Corsin Battaglia, and Meike V. F. Heinz\**

High-temperature sodium-nickel chloride (Na-NiCl$_2$) batteries are a promising solution for stationary energy storage, but the complex tubular geometry of the solid electrolyte represents a challenge for manufacturing. A planar electrolyte and cell design is more compatible with automated mass production. However, the planar cell design also faces a series of challenges, such as the management of molten phases during cycling. As a result, cycling of planar high-temperature cells until now focused on moderate areal capacities and current densities. In this work, planar cells capable of integrating cost-efficient nickel/iron electrodes at a substantially enhanced areal capacity of 150 mAh cm$^{-2}$ is presented. Due to a low cell resistance during operation at 300 °C, these cells deliver a specific discharge energy of 300 Wh kg$^{-1}$ at high discharge current densities of 80 mA cm$^{-2}$ (C/2, 10%–100% state-of-charge). This results represent the first demonstration of planar Na-NiCl$_2$ cells at a commercially relevant combination of areal capacity, cycling rate, and energy efficiency. It is further identified the secondary molten NaAlCl$_4$ electrolyte to contribute to the cell capacity during cycling. Mitigating electrochemical decomposition of NaAlCl$_4$ will play an important role in further enhancing both cycling rates and cycle life of high temperature Na-NiCl$_2$ batteries.

## 1. Introduction

The integration of intermittent renewable energy, such as wind and solar energy, requires stationary energy storage to balance supply and demand.[1–3] High-temperature sodium-nickel chloride (Na-NiCl$_2$) batteries, operated at temperatures of 300±40 °C, represent a promising solution for stationary energy storage, thanks to their long-term stability, high energy efficiency, and availability of sustainable raw materials.[4,5]

Commercial Na-NiCl$_2$ battery cells feature a complex 3D design, which is based on a tubular solid electrolyte with closed bottom, made from ceramic Na-$\beta''$-alumina.[6] The cells are assembled in the discharged state in the absence of Na metal. The solid positive electrode composite, consisting of Ni, Fe, NaCl, and various additives, is filled into the tubular ceramic electrolyte, where it is immersed in the secondary molten salt electrolyte NaAlCl$_4$ to enable mass transport. Molten Na is generated upon charge, covering the outer surface of the tubular electrolyte, where it is evenly distributed by a combination of wetting layers and metal shims.[6] Shaped at an aspect ratio (length/diameter) of more than 5,[6,7] the tubular design facilitates hermetic cell closure, as the sealed area is restricted to the circumference of the solid electrolyte tube at the open end. Advanced manufacturing processes applied during assembly of commercial Na-NiCl$_2$ cells provide durable hermetic seals. Combined with an optimized design of current collectors, commercial cells efficiently manage the molten phases present at both electrodes, thereby enabling a long battery design life of 20 years and more than 4500 cycles.[6] To reduce processing costs, commercial Na-NiCl$_2$ batteries contain tubular cells of significant size ($\approx$260 cm$^2$ active area) and capacity ($\approx$40 Ah, 150 mAh cm$^{-2}$).[8] In this geometry, typical charge and discharge rates of C/8 and C/3 translate into high charge and discharge current densities of 20 and 50 mA cm$^{-2}$, respectively.[14] Nevertheless, a low cell resistance of less than 4 Ω cm$^2$ (i.e., less than 15 mΩ at 260 cm$^2$)[7] enables commercial tubular Na-NiCl$_2$ batteries to deliver energy efficiencies of $\approx$90%.[9]

More recently, an alternative planar cell design has been introduced, with a series of achievements made on structural design, material selections, and operating conditions for

T. Lan,[+] G. Graeber,[++] L. Sieuw, E. Svaluto-Ferro, C. Battaglia,
M. V. F. Heinz
Empa
Swiss Federal Laboratories for Materials Science and Technology
Ueberlandstrasse 129, 8600 Dübendorf, Switzerland
E-mail: Meike.Heinz@empa.ch
F. Vagliani, D. Basso, A. Turconi
Fiamm Sonick Sa
Via Laveggio 15, 6855 Stabio, Switzerland

The ORCID identification number(s) for the author(s) of this article can be found under https://doi.org/10.1002/adfm.202302040.

[+]Present address: Materials Genome Institute, Shanghai University, Shanghai 200444, China

[++]Present address: Department of Chemistry, Humboldt-Universität zu Berlin 12489, Berlin, Germany

**ADVANCED
SCIENCE NEWS**

www.advancedsciencenews.com

**ADVANCED
FUNCTIONAL
MATERIALS**

www.afm-journal.de

Na-NiCl$_2$ batteries.[10,11,20–22,12–19] A planar cell design simplifies component manufacturing and assembly of high-temperature cells, making Na-NiCl$_2$ batteries more compatible with automated high-volume manufacturing and quality control routines.[1–3] The resulting decrease in processing costs is of central importance in view of the growing demand for low-cost stationary energy storage and the increasing pressure on the raw materials supply chain of lithium-ion batteries. The ability of planar cells to quickly accommodate modified active and passive components further enables research on numerous enhanced Na-NiCl$_2$ components. However, the planar cell design also faces a series of challenges. Compared to tubular cells, planar cells require a larger sealing area, making them more vulnerable to mechanical stresses, which result from volume changes caused by thermal and electrochemical processes.[23] At laboratory scale, cell sealing and an efficient management of the corrosive molten phases (molten NaAlCl$_4$ at the positive electrode, molten Na at the negative electrode) are technically challenging. As a result, extended cycling of planar Na-NiCl$_2$ cells until now focused on small cells (≈3 cm$^2$) with moderate areal capacities (≈50 mAh cm$^{-2}$).[13–15,18,24–26] The highest cycle life and cumulative capacity cycled in planar Na-NiCl$_2$ cells so far amounts to 200 cycles, ≈8 Ah cm$^{-2}$ at 280 °C (areal capacity ≈50 mAh cm$^{-2}$, ≈14–95% SOC), and to 1000 cycles, ≈43 Ah cm$^{-2}$ at 190 °C (areal capacity ≈50 mAh cm$^{-2}$, ≈13–99% SOC).[26] Polymer seals have been considered to facilitate the assembly and sealing of planar cells.[13–15,18,24,26,27] However, polymer seals restrict operation to reduced temperatures (≤200 °C), thereby increasing the cell resistance, which is significantly influenced by thermally activated processes.[21,25] Considering the high areal capacities required for stationary applications, a low cell resistance is of paramount importance to provide a high energy efficiency at relevant charge/discharge rates.

The electrochemical conversion reaction of the active cathode materials Ni, Fe, and NaCl in molten NaAlCl$_4$ electrolyte takes place within the electrochemical stability range of all components.[6,7] Unlike lithium-ion cells, which are often cycled between a lower and upper cutoff voltage, Na-NiCl$_2$ cells are commonly charged and discharged with a fixed capacity per cycle, which is supplied over a large part of battery life.[18,24,25] Therefore, capacity retention and coulombic efficiency, often discussed for lithium-ion batteries, are not an appropriate performance metric for Na-NiCl$_2$ cells for which voltage efficiency and energy efficiency are more relevant.

In this work, we present a substantially enhanced planar high-temperature battery cell platform, which for the first time matches the commercial tubular design in both areal capacity and energy efficiency. This important breakthrough is enabled by several rationally designed passive cell components that effectively manage the corrosive molten phases in the cells also at high mass loading. We demonstrate stable cycling of planar cells with state-of-the art Ni/Fe electrodes with an areal capacity of 150 mAh cm$^{-2}$ at discharge current densities of up to 80 mA cm$^{-2}$ (>C/2), corresponding to what is employed in commercial tubular cells, while being based on a planar cell design. In contrast to previous works on cells with low areal capacity, the thicker positive electrodes in our cells also enable a detailed microstructural analysis as a function of electrode depth, which unveils the secondary electrolyte NaAlCl$_4$ to supply NaCl during cycling. We then discuss the performance of the planar Na-NiCl$_2$ cells by relating their discharge energy, energy efficiency, areal capacity, and discharge current density. Extraction of an average cell resistance allows us to estimate the performance of cycling data in terms of discharge energy and energy efficiency at common conditions, such as those applied in commercial tubular cells.

## 2. Results

We previously developed a planar high-temperature battery cell platform, which enabled stable cycling of Na-NiCl$_2$ full cells with pure Ni and mixed Ni/Fe cathodes at 50 mAh cm$^{-2}$ areal capacity using disc-shaped current collectors.[25,28] However, when increasing the areal capacity to 150 mAh cm$^{-2}$, stable voltage profiles were obtained only for a few cycles, and the cells were unable to discharge the target capacity after a few initial cycles (see Figure S1, Supporting Information). Disassembly of the failed cells revealed leakage of Na, which emerged behind the current collector in the cells. Based on the theoretical density of molten Na at 300 °C (0.88 g cm$^{-2}$), the thickness changes at the negative electrode during cycling reach up to 0.5 mm at 50 mAh cm$^{-2}$, and up to 1.5 mm at 150 mAh cm$^{-2}$ areal capacity. At the higher areal capacity, disc-shaped current collectors are not reliable to manage the volume change of Na at the negative electrode of planar cells reversibly.

To avoid Na leakage in planar cells, we employ a corrugated current collector with Na storage capability at the negative electrode in this study. As shown in **Figure 1**a, the corrugated surface was designed to manage the volume change of molten Na during cycling, while establishing electrical contact at all states-of-charge (SOC). Square columns, with 1 mm side length and 3 mm height, are distributed homogenously on the current collector, with 1 mm gap in-between columns. The gaps provide a total volume of 700 mm$^3$ for molten Na (450 mm$^3$ required to accommodate 150 mAh cm$^{-2}$ Na at 300 °C), while the columns maintain electrical contact on the negative electrode, regardless of the Na volume change with SOC. The current collector was made of aluminum, and its surface was anodized to create a sodiophobic, i.e., sodium-repellant, aluminum oxide finish that enables complete retrieval of Na during discharge. Successful insertion and retrieval of molten Na is demonstrated visually in Figure 1b,c (Video S1, Supporting Information). Here, a drop of Na was pressed into the pore space of the corrugated current collector by an advancing piston. Upon removal of the piston, all Na was retrieved at the surface of the corrugated current collector.

We further demonstrated the electrochemical functionality of the new current collector design in a symmetric cell, comprising Na electrodes and corrugated current collectors on both sides of a planar, ceramic Na-$\beta''$-alumina electrolyte (BASE, Figure 1d). To resemble typical operation conditions in commercial tubular Na-NiCl$_2$ cells, we plated and stripped a capacity of 150 mAh cm$^{-2}$ molten Na per half cycle at 300 °C, applying current densities between 30 and 80 mA cm$^{-2}$. Symmetric cells with corrugated current collectors were cycled at stable overpotentials for >21 days, transferring a cumulative capacity of 16 Ah cm$^{-2}$ during 106 cycles. Based on the cell
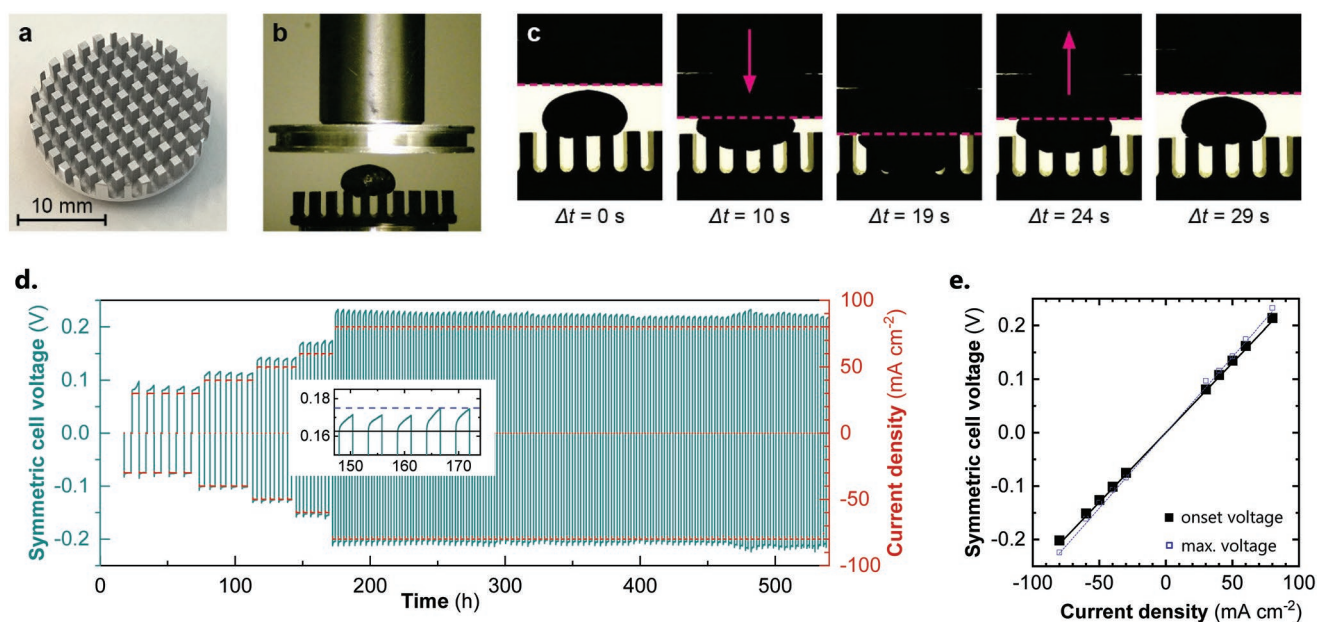
**Figure 1.** Design and performance of the corrugated current collectors. a) Current collector with Na storage capability, enabling reversible stripping and plating of molten Na electrode with 150 mAh cm$^{-2}$ areal capacity. b,c) Mechanical insertion and retrieval of a molten Na droplet in and from the corrugated current collector driven by the vertical movement of a piston. In (c), pink arrows indicate the direction of travel of the piston and $\Delta t$ represents the time between the first frame and the respective frame. d) Electrochemical cycling of a symmetric Na| BASE| Na cell, using corrugated current collectors for both electrodes (operation temperature: 300 °C, capacity per half cycle: 150 mAh cm$^{-2}$). In total, a cumulative half-cycle capacity of 16 Ah cm$^{-2}$ was transferred in 106 cycles. e) The cell voltage at the onset and the maximum cell voltage of each current pulse (inset in c) is used to estimate the cell resistance ($R_{cell}$ = 2.6 Ω cm$^2$), as well as additional contributions from the Na electrodes ($R_{IF} \leq 0.2$ Ω cm$^2$).

voltage that evolves at the onset of each current step, we estimate a cell resistance $R_{cell}$ of 2.6 Ω cm$^2$ (Figure 1e; Figure S2, Supporting Information). We further evaluate the maximum cell voltage for each set of current pulses, which represents additional interfacial and mass transport processes at the Na electrodes ($R_{cell+IF}$ = 2.8 Ω cm$^2$). Thus, mass transport of an equivalent of 150 mAh cm$^{-2}$ Na contributes a resistance of $R_{IF} \leq 0.2$ Ω cm$^2$. The capacity transferred per half cycle in this experiment significantly exceeds that reported in a previous study with disc-shaped current collectors with 25 mAh cm$^{-2}$ capacity per half cycle, where the cell resistance amounted to 1.3 Ω cm$^2$ at 250 °C.[28] Further design enhancements should focus on reducing the resistance contribution, as well as mass and volume of Na current collectors with Na storage capability, for example by applying a conductive felt or sponge. Nevertheless, these symmetrical cell experiments demonstrate the ability of the corrugated current collector to manage molten Na at relevant half-cycle capacity and current density.

Next, we assembled planar Na-NiCl$_2$ full cells comprising a corrugated current collector at the negative electrode, and mixed Ni/Fe granules at an areal capacity of 150 mAh cm$^{-2}$ at the positive electrode. As common for Na-NiCl$_2$ cells, we applied a combined constant-current and constant-voltage (CC-CV) routine during charge and discharge, with upper and lower cut-off voltages of 2.68 and 1.80 V, respectively. Stable cycling was achieved at 300 °C between 10% and 100% state-of-charge (SOC, cycled capacity 137 mAh cm$^{-2}$), as shown exemplarily for one cell in **Figure 2**. The first, or maiden, cycle of the cell includes irreversible reactions and is presented in Figure S3a (Supporting Information). We then cycled the cell in two steps:

in the first step (Figure 2a), symmetrical charge and discharge current densities (5, 10, 15, and 20 mA cm$^{-2}$) were applied. The voltage-capacity curves indicate two voltage plateaus for Ni and Fe chlorination. These are separated by a transition region, which involves the contribution of additives (FeS, NaF).[19,25,29] The cell voltage gradually increases in the transition region during the first few cycles due to microstructural stabilization of the mixed Ni/Fe electrode.[25,30,31] In the following cycles, the voltage-capacity curves at a given current density overlap. Stable cycling was also achieved in the second step (Figure 2b), where we limited the charge current density to 20 mA cm$^{-2}$, but discharged the cell at higher current densities (30, 40, 50, and 80 mA cm$^{-2}$). The operation conditions applied in Figure 2b are typical for commercial tubular Na-NiCl$_2$ cells, with charge limited at a current density of 20 mA cm$^{-2}$ and by a cut-off voltage of 2.68 V to avoid side reactions.[7,9] The charge and discharge energies of all cycles are summarized in Figure 2c, together with the corresponding energy efficiencies. Applying a CC-CV routine during charge, the cell successfully cycled in the chosen SOC window between 10% and 100% SOC, resulting in a coulombic efficiency of 100% in all cycles. Thus, during charge and discharge cycling, only the cell voltages fade, which affects the voltage efficiency and consequently also the energy efficiency. During most cycles plotted in Figure 2c, the cell shows a stable performance with constant energy efficiency at each current density. The energy efficiency is 97% at 5 mA cm$^{-2}$ charge and discharge current densities. The energy efficiency decreases with higher polarization introduced by higher current densities, to 82% in cycles with 20 mA cm$^{-2}$ charge and 80 mA cm$^{-2}$ discharge current densities; but the energy efficiency recovered
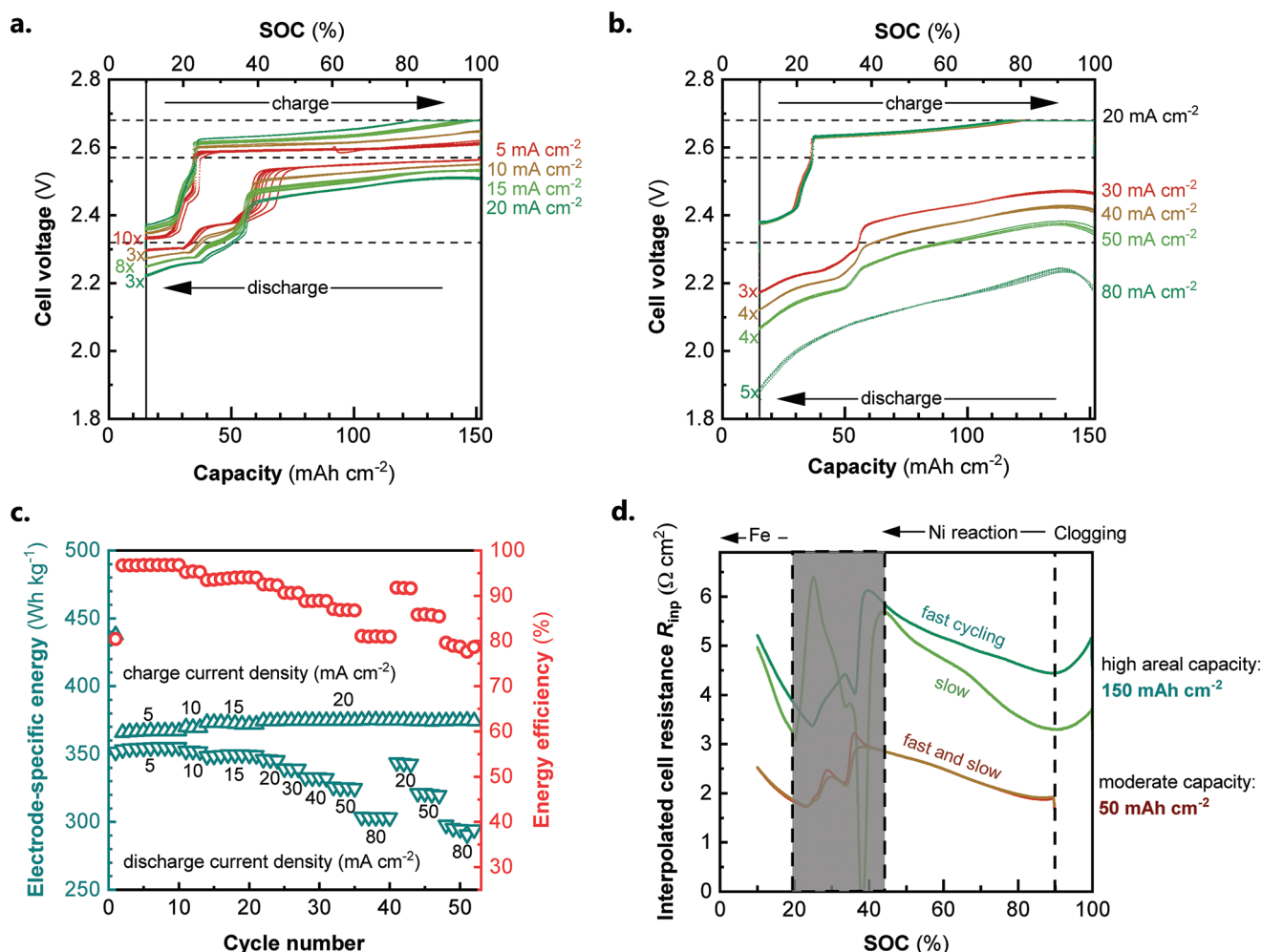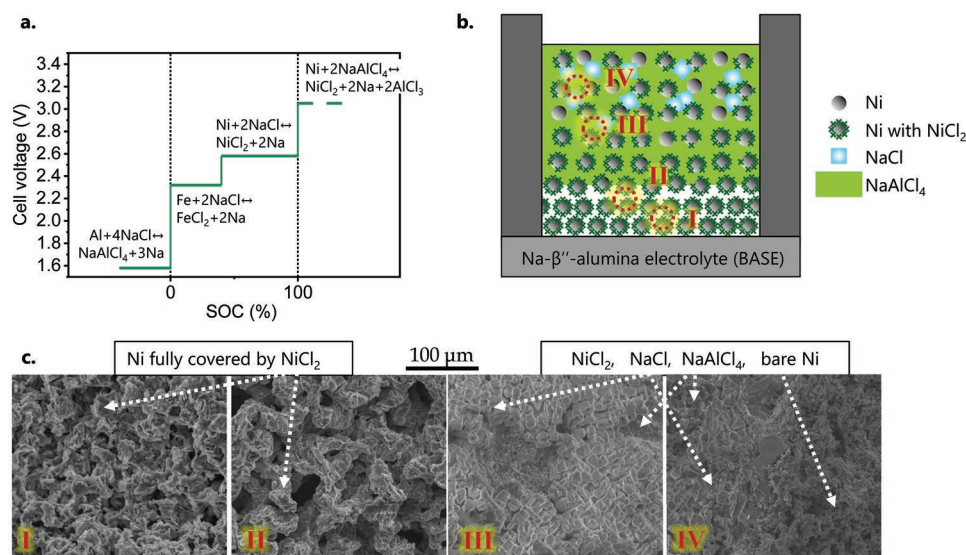
**Figure 2.** Performance of a mixed Ni/Fe cell with 150 mAh cm$^{-2}$ areal capacity at 300 °C, with upper cut-off voltage at 2.68 V. a) Cycling with symmetrical charge and discharge current densities (3-10 cycles at 5, 10, 15, and 20 mA cm$^{-2}$). b) Consecutive cycling with 20 mA cm$^{-2}$ charges current density and higher discharge current densities (3–5 cycles at 30, 40, 50, and 80 mA cm$^{-2}$). c) Electrode-specific charge/discharge energies and energy efficiency at variable current densities (5–80 mA cm$^{-2}$) for 52 cycles (cumulative capacity 7 Ah cm$^{-2}$). In total, 60 cycles were completed between 10% and 100% SOC (cumulative capacity 8 Ah cm$^{-2}$, see Figure S3c, Supporting Information). d) Interpolated cell resistance of cells with high (150 mAh cm$^{-2}$) and moderate (50 mAh cm$^{-2}$) areal capacity, $R_{inp}$, as a function of SOC. Read from right to left to follow discharge reactions. $R_{inp}$ is calculated from linear interpolation of the discharge voltage curves in a, b at variable current densities. Fast cycling corresponds to charge at 20 mA cm$^{-2}$, discharge at 20–50 mA cm$^{-2}$; slow cycling corresponds to symmetrical charge and discharge at 5–20 mA cm$^{-2}$.

in following cycles at lower current densities (cycle 41–43), showing that the previous decrease was only the effect of polarization caused by cell resistance. Only minor degradation occurred in the energy efficiency at high discharge current densities after cycle 43, compared to previous cycles. We even performed additional cycles at a discharge current density of 120 mA cm$^{-2}$ (cycle 53–60, cumulative capacity 8 Ah cm$^{-2}$, Figure S3b,c, Supporting Information). However, this current density could not be maintained during discharge, and the lower cut-off potential was reached below 70% SOC.

In Figure 2d, we apply linear interpolation between the discharge voltage curves (Figure 2a,b) to calculate the SOC-dependent cell resistance ($R_{inp}$) of planar cells with mixed Ni/Fe electrode and 150 mAh cm$^{-2}$ areal capacity (corrugated current collector). For reference, we also present the corresponding data for cells with a lower areal capacity of 50 mAh cm$^{-2}$

(disc-shaped current collectors). Errors in both calculations are given in Figure S4 (Supporting Information). The cells with low areal capacity (50 mAh cm$^{-2}$) feature an ohmic cell resistance of up to 2.8 Ω cm$^{2}$.[25] Constant (SOC-independent) resistance contributions, 1.7 Ω cm$^{2}$ in total, are ascribed to the ceramic BASE (thickness 1 mm, 0.2 S cm$^{-1}$ at 300 °C), to passive cell components (cell case, cables, disc-shaped current collectors, etc.), to the negative Na electrode, and to the electronic backbone of the positive electrode (see Figure S5a, Supporting Information). The SOC-dependent resistance contributions are assigned to mass transport in the positive electrode, where the cell resistance increases upon discharge as electrochemical conversion progresses along separate reaction fronts for Ni and for Fe. With 50 mAh cm$^{-2}$ areal capacity, linear interpolation of discharge curves at variable current densities (slow or fast cycling, at 6–20 or 20–50 mA cm$^{-2}$) gives very similar results.

**2302040 (4 of 9)**

**ADVANCED
SCIENCE NEWS**

www.advancedsciencenews.com

**ADVANCED
FUNCTIONAL
MATERIALS**

www.afm-journal.de

**Figure 3.** SEM analysis for a cycled cell. a) Electrochemical reactions reported for mixed Ni/Fe cells at 300 °C, with dash lines representing postulated reactions.[6,7,9] b) Location of sample positions I-IV in the positive electrode (post-mortem, at 100% SOC), and schematic results of SEM analysis (percolation of metal particles not shown here for clarity). c) Representative SEM images taken at sample positions I-IV.

Discrepancies only arise in the transition region, where the current density influences the onset of additive reactions and Fe dechlorination. The interpolated cell resistance of the present 150 mAh cm$^{-2}$ cells is about twice that of 50 mAh cm$^{-2}$ cells (Figure 2d). It also increases along separate reaction fronts for Ni and Fe upon discharge but shows a more complex behavior. With a higher areal capacity, SOC-independent resistance contributions amount to 3.1 Ω cm$^2$, which increase to 6.0 Ω cm$^2$ including SOC-dependent contributions (see Figure S5b, Supporting Information). The SOC-independent contribution is dominated by the negative Na electrode and the corrugated current collector, which leave room for further design enhancements. Furthermore, $R_{inp}$ differs for different current density ranges (slow or fast cycling, Figure 2d), indicating deviation from an ohmic behavior. While the resistances converge toward the end of a reaction front (e.g., 5.7 Ω cm$^2$ at 45% SOC), much lower values are obtained at the beginning of discharge during slow cycling (e.g., 3.2 Ω cm$^2$ at 90% SOC), compared to fast cycling (4.5 Ω cm$^2$ at 90% SOC). Thus, additional effects add to the reaction front mechanism in the thicker positive electrode, leading to a non-ohmic cell resistance. We further observe an unexpected behavior for 150 mAh cm$^{-2}$ cells at the beginning of discharge between 100% and 90% SOC. Upon discharge, the cell voltage starts at relatively low values, but gradually increases until ≈90% SOC are reached (Figure 2b). This corresponds to a decreasing cell resistance between 100% and 90% SOC (Figure 2d), which becomes more pronounced at higher current densities. Such behavior is in line with an inhomogeneous positive electrode microstructure developed during the previous charge, which temporarily deteriorates mass transport through molten NaAlCl$_4$ by a clogging effect.[25] In particular, preferential formation of NiCl$_2$ close to the ceramic electrolyte could hinder ionic transport through NaAlCl$_4$, thereby increasing the mass transport resistance at the beginning of the discharge.

After cycling shown in Figure 2 and Figure S3b,c (Supporting Information), we characterized the fully charged positive electrode (100% SOC) of the cell postmortem by scanning electron microscopy (SEM) (**Figure 3**). Considering the cell voltage range applied during cycling (1.80–2.68 V, Figure 2a,b), the electrochemical reactions in our cell are restricted to the de-/chlorination of Ni and Fe at ≈2.6 and ≈2.3 V according to literature (Figure 3a).[6,7] Thus, at 100% SOC, the positive electrode is expected to consist of NiCl$_2$ and FeCl$_2$ (or Ni$_{1-x}$Fe$_x$Cl$_2$[32]), NaAlCl$_4$ electrolyte, and excess Ni, with all NaCl being consumed by the chlorination of Fe and Ni. By collecting electrode fragments from a defined depth in the electrode and transferring them to the microscope in inert atmosphere, we analyzed composition and microstructure as a function of depth, in the presence of the secondary NaAlCl$_4$ electrolyte (Figure 3b). In this way, we identified the presence of all expected phases in the positive electrode (simplified as NiCl$_2$, NaAlCl$_4$, and Ni in Figure 3c). However, the presence of NaCl is detected as well, and both microstructure and phase content vary significantly at different positions in the positive electrode. Near the Na-$\beta''$-alumina electrolyte (BASE) at position I and II Figure 3c, the entire electrode surface is covered by NiCl$_2$ with flake-shaped morphology, similar to previous reports on heavily chlorinated planar Ni model electrodes.[33] However, no NaAlCl$_4$ is present at position I and II according to EDS, and the electrode porosity is much higher close to the BASE, compared to further away. This indicates severe NaAlCl$_4$ loss, which is likely to have caused cell degradation after cycle #50. Furthermore, the microstructures differ at positions I and II, with smaller porosity and narrower pore channels at position I. Moving to the middle of the electrode at position III and IV, NaAlCl$_4$ is present, surrounding other phases. Furthermore, NaCl particles are identified at position III and IV. At position IV, bare Ni is present, which was not converted to NiCl$_2$. Thus, the phase distribution at the positive electrode is inhomogeneous after cycling: close

**ADVANCED
SCIENCE NEWS**

www.advancedsciencenews.com

**ADVANCED
FUNCTIONAL
MATERIALS**

www.afm-journal.de

to the BASE, the porosity is reduced and $NaAlCl_4$ is depleted, as Ni is heavily chlorinated into $NiCl_2$; further away, unreacted Ni and NaCl are present in the fully charged state. These inhomogeneities are caused by gradual mass transport in the positive electrode during cycling, during charge. Preferential Ni chlorination and reduced porosity/$NaAlCl_4$ close to the BASE affect the SOC dependent cell resistance by reducing mass transport and altering the reaction front and corresponding active surface sites during slow and fast cycling (Figure 2d). Furthermore, the combination of $NaAlCl_4$ loss close to the BASE with the presence of NaCl further away indicates decomposition and partial electrochemical consumption of $NaAlCl_4$ during cell cycling. According to literature, the so-called overcharge reaction between Ni and $NaAlCl_4$ into Na, $NiCl_2$, and volatile $AlCl_3$ is generally assumed to take place at 3.05 V, well above the cell voltage applied in this experiment (Figure 2b).[6,7,9] However, the existence of NaCl at 100% SOC has previously been reported also for commercial tubular cells, where it was partially ascribed to solubility changes upon cooling to room temperature.[34] In order to further investigate a possible reaction involving $NaAlCl_4$ at common $Na-NiCl_2$ cycling conditions, we prepared a NaCl-free model cell. As shown in Figure S6 (Supporting Information), this cell delivered a capacity of up to 35 mAh in the Ni plateau when cycled up to 2.72 V. This experiment confirms active participation of $NaAlCl_4$ in the chlorination reactions well below 3.05 V. We further ascribe the fast capacity fading of this model cell to formation of $AlCl_3$, which is highly volatile at 300 °C and displaces $NaAlCl_4$ at the reaction sites. Under normal $Na-NiCl_2$ cycling conditions, the Ni charge reaction with NaCl is preferred over the overcharge reaction with $NaAlCl_4$ reaction. However, both reactions can take place ≤2.68 V, depending on the availability of NaCl and the magnitude of cell overpotentials. Consequently, a low cell resistance is beneficial not only for energy efficiency, but also for the lifetime of $Na-NiCl_2$ batteries, at high areal capacity.

$Na-NiCl_2$ cells are best compared in terms of discharge energy and energy efficiency. Naturally, these values strongly depend on cycling conditions and cell design, especially on areal capacity and current density, which vary significantly in different studies. They are further affected by the electrode composition, by the choice of active metal and by the mass ratio of metal to rock salt in the positive electrode, indicating the active metal content. **Figure 4** provides an overview on the published performance of planar $Na-NiCl_2$ cells (see Figure S7 and Table S1 for details on data compilation, Supporting Information), with Figure 4a,b visualizing the effects of areal capacity and current density on the electrode-specific discharge energy for the same data set.[13–15,18,24–27] The cycled areal capacity results from the specific capacity (mAh $g^{-1}$) and mass loading (g $cm^{-2}$) of the positive electrode materials, as well as from the state-of-charge (SOC) range accessed during cycling (Figure 4a). In most previous studies, the cycled areal capacities ranged between 30 and 50 mAh $cm^{-2}$ (Figure 4a), applying pure Ni as active metal at the positive electrode at active contents below 30% (mass ratio of Ni to NaCl ≈1.8).[13–15,18,24,26,27] The highest discharge energy of 405 Wh $kg^{-1}$ was reported for electrodes with increased active Ni content of 40% (mass ratio of Ni to NaCl = 1.25) at an areal capacity of ≈65 mAh $cm^{-2}$.[14] One previous study presented areal capacities up to 125 mAh $cm^{-2}$, but
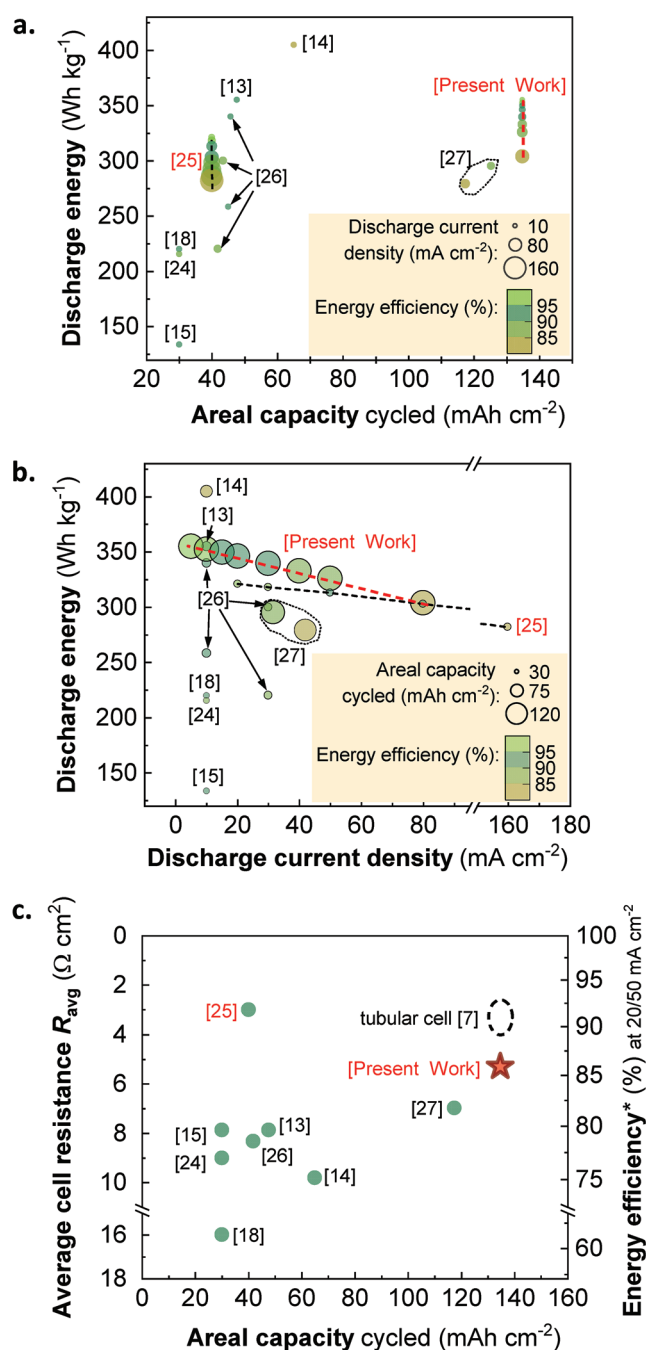


**Figure 4.** Performance comparison of planar $Na-NiCl_2$ cells from the present work with literature results,[7,13–15,18,24,26,27] including our previous study applying a lower areal capacity.[25] a) Electrode-specific discharge energy plotted against area capacity cycled. Dot size and color represent discharge current density and energy efficiency, respectively. b) Electrode-specific discharge energy plotted against discharge current density, with dot size and color representing areal capacity cycled and energy efficiency. c) Average resistance, $R_{avg}$, calculated for different cells. This was used to estimate the corresponding energy efficiency at typical $Na-NiCl_2$ battery cycling conditions (charge at 20 mA $cm^{-2}$, discharge at 50 mA $cm^{-2}$, Ni reaction at 2.58 V).

demonstrated discharge energies below 300 Wh $kg^{-1}$ even at a moderate current density of 30 mA $cm^{-2}$.[27] In the present

work, we demonstrate cycling of the highest areal capacity so far, reaching discharge energies of up to 350 Wh kg$^{-1}$. Our data also compares favorably with literature when considering the dependence on current density. As shown in Figure 4b, the discharge energy of specific Na-NiCl$_2$ cells often decreases linearly with increasing current density, in line with an ohmic cell resistance.[25] Despite the high areal capacity cycled (137 mAh cm$^{-2}$), our present cells supplies high discharge energies also at high current densities (e.g., 300 Wh kg$^{-1}$ at 80 mA cm$^{-2}$). We relate the enhanced performance of our cells to a combination of low cell resistance and wide SOC range accessed during cycling. Cell resistance is important not only to achieve high discharge energies, but also for high energy efficiencies required for stationary energy storage applications. To compare the performance of planar cells from different reports (at various discharge current densities) directly, we estimated the average internal resistance, $R_{avg}$, of published reports based on their reported energy efficiency $\eta_{energy}$ (Equation 1). During cycling in a defined SOC range (100% CE), this equals to the ratio of polarized discharge and charge voltages of the cell.

$$\eta_{energy} = \frac{V_{eq} - I_{discharge}R_{avg}}{V_{eq} + I_{charge}R_{avg}}; \quad R_{avg} = \frac{V_{eq}\left(1 - \eta_{energy}\right)}{I_{charge}\eta_{energy} + I_{discharge}} \quad (1)$$

where $\eta_{energy}$ is the energy efficiency, $I_{charge/discharge}$ is the charge/discharge current density, and $V_{eq}$ is the equilibrium potential (2.58 V for Ni-NiCl$_2$ reaction, 2.49 V for mixed Ni-Fe cells). We further applied $R_{avg}$ to assess the effect of cell resistance on the energy efficiency at typical Na-NiCl$_2$ cycling conditions, corresponding to charge at C/8, 20 mA cm$^{-2}$, and discharge at C/3, 50 mA cm$^{-2}$ (assuming ohmic behavior). As summarized in Figure 4c, many previous cells suffer from high cell resistances ≥ 8 Ω cm$^2$, despite low areal capacities. At typical Na-NiCl$_2$ cycling conditions, this results in low energy efficiencies ≤80%. In contrast, our present cells achieve >85% energy efficiency at $R_{avg}$ < 6 Ω cm$^2$, despite their higher areal capacity. For planar Na-NiCl$_2$ cells, lower cell resistances have only been demonstrated in our previous study with lower areal capacity.[25] In fact, this study is the first demonstration of cost-efficient planar Na-NiCl$_2$ cells with a cycling performance like that of state-of-the-art tubular cells. State-of-the-art tubular Na-NiCl$_2$ cells achieve energy efficiencies > 90% with an optimized cell design and commercially engineered production process.[7,9] Further enhancements to the design of planar cells can be easily achieved by reducing weight, volume and electrical resistance of passive cell components (such as the current collectors and cell case).

## 3. Conclusion

The present work constitutes a central step towards the wide deployment of high-temperature Na-NiCl$_2$ batteries, and thereby for more sustainable electrochemical energy storage. For the first time, we show planar prototype cells that can achieve a competitive electrochemical performance comparable to their commercial tubular cell counter parts. The presented cells deliver a high areal capacity of 150 mAh cm$^{-2}$, combined with a specific energy of 300 Wh kg$^{-1}$, a current density of up

to 80 mA cm$^{-2}$, and an energy efficiency ranging between 82% and 97%, thereby outperforming all previously reported planar cells. Most importantly, these results were obtained at 300 °C using a simple, planar cell design. In contrast to the commercial tubular cells, such planar cells facilitate cost-effective, automated production. To enable this outstanding performance, we designed cells that feature corrugated sodiophobic current collectors for efficient storage and release of molten Na during cycling. It can be expected that more research related to the storage and release of the molten alkali metal will enable further enhancements in the areal capacity of planar cells, thereby also surpassing state-of-the-art tubular cells. To obtain insights into the electrochemical processes in Na-NiCl$_2$ cells, at high areal capacity, we combined model cell experiments and micro-structural analyses. Furthermore, we present different methods to assess the cell resistance, and discuss its importance on the performance of Na-NiCl$_2$ cells at relevant operating conditions. These advances can guide the rational design of economically viable Na-NiCl$_2$ cells, which profit from enhanced discharge energy and energy efficiency at elevated temperatures. Further research and development need to address practical challenges to reduce weight and volume of passive cell components, further reduce cell resistance, and enhance cell sealing. Once these steps are achieved, Na-NiCl$_2$ can serve as the primary solution to numerous stationary storage needs related to the integration of renewables and the global push toward a net-zero economy. At present, the cycle life of custom-made planar high-temperature battery cells does not meet that achieved in commercial tubular cells, which apply optimized cell components and hermetic seals. However, our study demonstrates the benefits of applying current collectors as an anode reservoir. This approach not only boosts the development of planar high-temperature Na-NiCl$_2$ cells, but it may also be applied in the design of metal-anode batteries operated at ambient temperature.
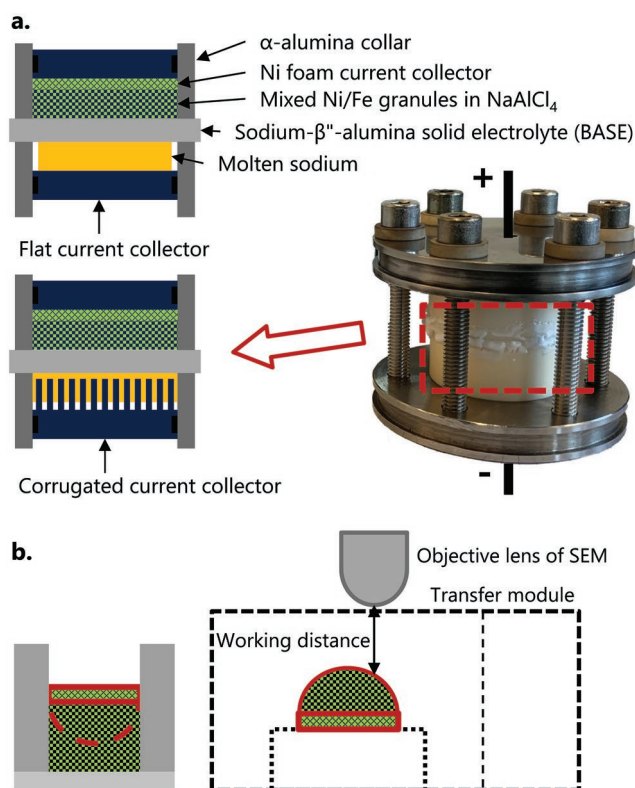
## 4. Experimental Section

*Material Fabrication*: Sodium-$\beta''$-alumina solid electrolyte (BASE) disks were produced by sintering pressed pellets, as reported in a previous paper.[35] Li-stabilized Na-$\beta''$-alumina powder was pressed into green bodies (45 mm diameter, ≈4 mm thickness) with a uniaxial pressure of 60 MPa. The green bodies were sintered on a Na-$\beta''$-alumina powder bed with a ceramic encapsulation in static air at 1600 °C (Nabertherm HT 40/17, 3 K min$^{-1}$ heating rate, 5 min dwell time). Sintered BASE discs were polished to a thickness of 1 mm (Elb surface grinding machine) and dried at 100 °C to avoid H$_2$O contamination.

Mixed Ni/Fe granules, comprising the active materials of the positive electrode, were made of Ni (50.4 wt.%, filamentary Ni255), Fe (6.6 wt.%), NaCl (39.0 wt.%), and additive powders (Al 0.5 wt.%, FeS 1.6 wt.%, NaF 1.5 wt.%, NaI 0.4 wt.%) using a roller press (Komarek B050A, roll force 30 kN) and a granulator (Komarek G100SA). As detailed previously, this composition translates to a reversible electrode capacity of 159 mAh g$^{-1}$ (100% SOC), with 60% SOC available from Ni de-/chlorination at 2.57 V, and 40% SOC available from Fe de-/chlorination at 2.32 V.[25] During reversible cycling, the mass ratio of Ni+Fe to NaCl amounts to 1.65, corresponding to an overall active metal content of 30% (Fe 100% active, Ni 20.7% active; 11.5% NaCl used for irreversible chlorination of Al).

*Cell Fabrication*: The planar high-temperature cell platform with 3.14 cm$^2$ active area comprises a ceramic subassembly, active electrode materials, current collectors, sealants, and other structural components (**Figure 5**a). The ceramic subassembly was prepared by sealing the BASE

**Figure 5.** Experimental setups. a) Design of planar high-temperature cells with disc-shaped and corrugated current collector at the negative electrode, respectively. b) Retrieval of SEM sample and reconstruction of its position in the positive electrode, maintaining the original microstructure (incl. solidified $NaAlCl_4$).

between two insulating $\alpha$-alumina collars using a high-temperature glass seal.[25] Then, a carbon coating was sprayed on one side of the solid electrolyte in the ceramic subassembly (7 wt.% carbon black, 11 wt.% sodium hexamethaphosphate, 55 wt.% isopropanol, 27 wt.% water, and 0.3 wt.% acetone) using an airbrush system (Aztek, ≈2 bar pressurized air) and drying in air (Carbolite CWF 1200, 5 K min$^{-1}$ to 280 °C, 5 min dwell time). The carbon coating enhances the wetting of molten Na.[28] In symmetric Na| BASE| Na cells, both sides of the solid electrolyte were coated. A K-type thermocouple was attached onto one of the $\alpha$-alumina collars to measure the cell temperature.[25]

Disc-shaped current collectors (for the positive electrode in full cells) were made of Ni discs (diameter 2 cm). Corrugated current collectors (for the negative electrode) were machined from Al (diameter 2 cm, square columns with 1 mm side length and 3 mm height, 1 mm gap in-between columns) and subsequently anodized. The endplates closing both sides of the ceramic subassembly were machined out of stainless steel, with graphite O-rings between endplates and $\alpha$-alumina collar.

The cells were assembled inside an Ar-filled glovebox. 3 g granules were added into the ceramic subassembly, on the side without carbon coating (0.955 g cm$^{-2}$, 152 mAh cm$^{-2}$, thickness ≈7 mm). 1.5 g $NaAlCl_4$ (Sigma–Aldrich) were infiltrated into the granules at a pressure of <10 mbar at 200 °C. A Ni foam (Goodfellow, 1.6 mm thickness, 95% porosity) and additional 0.3 g of $NaAlCl_4$ were added to the positive electrode to maintain both electronic and ionic contact of the electrode composite during cell cycling, as reported previously.[25] A thin Na foil was pressed on the carbon coating at the negative electrode to facilitate the first (maiden) charge, and to compensate possible losses within the cell (≈20 mm diameter round disk, ≈0.3 g). Both current collectors were carefully inserted into the ceramic subassembly. The current collectors were mechanically connected to the endplates by springs to

compensate dimensional tolerances in different cells. Due to a tight fitting of the current collector inside the $\alpha$-alumina collar, the current collectors did not move or change position in the cell during cycling. Separate electrical connections by Ni wires and screws were inserted to reduce the cell resistance, and carbon felt strips (Sigratherm KFD 2) were inserted around the spring at the positive side. To close the cell, the endplates were compressed against the ceramic subassembly by six steel bolts, insulated with $\alpha$-alumina washers. Special cells, i.e., Na-Na symmetric cells and cells without NaCl, were assembled similarly. In Na-Na symmetric cells, Na disks (≈0.3 g for the initial plating side and ≈0.6 g for the initial stripping side) with corrugated current collectors were put into both sides of the ceramic subassembly. In cells without NaCl, only a Ni-foam and ≈0.6 g $NaAlCl_4$ were added to the positive side of the ceramic subassembly.

*Cell Tests*: Cells were electrochemically tested inside an Ar-filled glovebox. The charge-discharge behavior of the cells was measured by an electrochemical testing system (Biologic VMP-3e) at 300±10 °C, maintained by a glass fiber heating jacket and a resistive coil heater (SAF KM-HC-GS). For Na-Na symmetric cells, a constant current (CC) routine was applied with fixed areal capacity 152 mAh cm$^{-2}$ per half cycle. For full cells, a CC-CV (combined constant current and constant voltage) routine was applied between 10% and 100% SOC (cycled capacity 137 mAh cm$^{-2}$), with an upper cut-off voltage of 2.68 V to avoid Fe oxidation, and a lower cut-off voltage of 1.8 V to avoid $NaAlCl_4$ decomposition. In this SOC range, the mixed Ni/Fe electrode provides an average equilibrium cell voltage of 2.49 V (Fe reaction at 2.32 V from 10%–40% SOC, Ni reaction at 2.57 V from 40%–100% SOC).[25] For cells with only Ni foam and $NaAlCl_4$ in the positive electrode (without NaCl), a CC routine was applied between 2.48 and 2.64 V. Charge and discharge energies were derived as the time integral of cell voltage times current for CC-CV routines, or as the capacity integral of cell voltage for CC routines. Specific capacities and specific energies are stated per mass of active materials (i.e., mass of positive electrode granules). During cycling of the cell in Figure 4a, a short power failure of the heater was experienced, which resulted in a temperature decrease and a fluctuation in 9th charge curve at 5 mA cm$^{-2}$.

*Characterization*: Scanning electron microscopy (SEM, Nova NanoSEM 230 FEI) with energy-dispersive X-ray spectroscopy (EDX) analysis was performed on raw materials, as well as on pristine and cycled cells. A transfer module (Kammrath and Weiss) was used to transfer samples from cycled cells into the SEM chamber under argon, avoiding reaction of $NaAlCl_4$ with $H_2O$ or $CO_2$ in ambient air. For a cycled cell, a single piece of fragment connected to the Ni foam was excavated from the positive electrode, which was transferred by the transfer module and placed inside the SEM. The relative depths of images was defined by the working distance of the SEM, as shown in Figure 5b. Positions II, III, and IV discussed in Figure 4 correspond to the cross-section of a single piece of positive electrode fragment connected to the Ni foam, which was obtained from the cell after cycling (post-mortem). Position I was from a separate fragment close to the BASE. In the analysis of SEM and EDS measurements, a volume reduction of $NaAlCl_4$ due to an increase in density upon cooling (1.60 g cm$^{-3}$ at 300 °C, 2.01 g cm$^{-3}$ at room temperature) was considered.[36]

## Supporting Information

Supporting Information is available from the Wiley Online Library or from the author.

## Acknowledgements

## Conflict of Interest

The authors declare no conflict of interest.

## Data Availability Statement

The data that support the findings of this study are openly available in Zenodo at https://doi.org/10.5281/zenodo.7625714, reference number 7625714.

[1] D. Larcher, J. M. Tarascon, *Nat. Chem.* **2015**, *7*, 19.

[2] B. Dunn, H. Kamath, J. M. Tarascon, *Science* **2011**, *334*, 928.

[3] Z. Yang, J. Zhang, M. C. W. Kintner-Meyer, X. Lu, D. Choi, J. P. Lemmon, J. Liu, *Chem. Rev.* **2011**, *111*, 3577.

[4] S. F. Schneider, C. Bauer, P. Novák, E. J. Berg, *Sustain. Energy Fuels* **2019**, *3*, 3061.

[5] C. Vaalma, D. Buchholz, M. Weil, S. Passerini, *Nat. Rev. Mater.* **2018**, *3*, 18013.

[6] J. L. Sudworth, *J. Power Sources* **2001**, *100*, 149.

[7] C. H. Dustmann, *J. Power Sources* **2004**, *127*, 85.

[8] V. Zinth, M. Schulz, S. Seidlmayer, N. Zanon, R. Gilles, M. Hofmann, *J. Electrochem. Soc.* **2016**, *163*, A838.

[9] R. Benato, N. Cosciani, G. Crugnola, S. Dambone Sessa, G. Lodi, C. Parmeggiani, M. Todeschini, *J. Power Sources* **2015**, *293*, 127.

[10] X. Lu, G. Coffey, K. Meinhardt, V. Sprenkle, Z. Yang, J. P. Lemmon, *ECS Trans.* **2010**, *28*, 7.

[11] X. Zhan, J. P. Sepulveda, X. Lu, J. F. Bonnett, N. L. Canfield, T. Lemmon, K. Jung, D. M. Reed, V. L. Sprenkle, G. Li, *Energy Storage Mater.* **2020**, *24*, 177.

[12] X. Zhan, J. F. Bonnett, M. H. Engelhard, D. M. Reed, V. L. Sprenkle, G. Li, *Adv. Energy Mater.* **2020**, *10*, 2001378.

[13] K. Jung, H. J. Chang, J. F. Bonnett, N. L. Canfield, V. L. Sprenkle, G. Li, *J. Power Sources* **2018**, *396*, 297.

[14] H. J. Chang, X. Lu, J. F. Bonnett, N. L. Canfield, S. Son, Y. C. Park, K. Jung, V. L. Sprenkle, G. Li, *Adv. Mater. Interfaces* **2018**, *5*, 1701592.

[15] H.-J. Chang, N. L. Canfield, K. Jung, V. L. Sprenkle, G. Li, *ACS Appl. Mater. Interfaces* **2017**, *9*, 11609.

[16] D. Y. Wang, C. Y. Wei, M. C. Lin, C. J. Pan, H. L. Chou, H. A. Chen, M. Gong, Y. Wu, C. Yuan, M. Angell, Y. J. Hsieh, Y. H. Chen, C. Y. Wen, C. W. Chen, B. J. Hwang, C. C. Chen, H. Dai, *Nat. Commun.* **2017**, *8*, 14283.

[17] G. Li, X. Lu, J. Y. Kim, V. V. Viswanathan, K. D. Meinhardt, M. H. Engelhard, V. L. Sprenkle, *Adv. Energy Mater.* **2015**, *5*, 1500357.

[18] G. Li, X. Lu, J. Y. Kim, J. P. Lemmon, V. L. Sprenkle, *J. Power Sources* **2014**, *249*, 414.

[19] G. Li, X. Lu, J. Y. Kim, M. H. Engelhard, J. P. Lemmon, V. L. Sprenkle, *J. Power Sources* **2014**, *272*, 398.

[20] G. Li, X. Lu, J. Y. Kim, J. P. Lemmon, V. L. Sprenkle, *J. Mater. Chem. A* **2013**, *1*, 14935.

[21] X. Lu, G. Li, J. Y. Kim, J. P. Lemmon, V. L. Sprenkle, Z. Yang, *J. Power Sources* **2012**, *215*, 288.

[22] G. Li, X. Lu, C. A. Coyle, J. Y. Kim, J. P. Lemmon, V. L. Sprenkle, Z. Yang, *J. Power Sources* **2012**, *220*, 193.

[23] M. V. F. Heinz, G. Graeber, D. Landmann, C. Battaglia, *J. Power Sources* **2020**, *465*, 228268.

[24] H. J. Chang, X. Lu, J. F. Bonnett, N. L. Canfield, S. Son, Y. C. Park, K. Jung, V. L. Sprenkle, G. Li, *J. Power Sources* **2017**, *348*, 150.

[25] G. Graeber, D. Landmann, E. Svaluto-Ferro, F. Vagliani, D. Basso, A. Turconi, M. V. F. Heinz, C. Battaglia, *Adv. Funct. Mater.* **2021**, *31*, 2106367.

[26] G. Li, X. Lu, J. Y. Kim, K. D. Meinhardt, H. J. Chang, N. L. Canfield, V. L. Sprenkle, *Nat. Commun.* **2016**, *7*, 10683.

[27] X. Lu, H. J. Chang, J. F. Bonnett, N. L. Canfield, K. Jung, V. L. Sprenkle, G. Li, *J. Power Sources* **2017**, *365*, 456.

[28] D. Landmann, G. Graeber, M. V. F. Heinz, S. Haussener, C. Battaglia, *Mater. Today Energy* **2020**, *18*, 100515.

[29] J. L. Sudworth, *J. Power Sources* **1994**, *51*, 105.

[30] T. Javadi-Doodran, *Microstructure and Conductivity of the Sodium Nickel Chloride (ZEBRA) Battery Cathode*, McMaster University, **2012**.

[31] R. Christin, *Multiphysics Modeling of Sodium Nickel Chloride Cells*, PhD Thesis, Grenoble Alpes University, **2015**.

[32] V. Zinth, S. Seidlmayer, N. Zanon, G. Crugnola, M. Schulz, R. Gilles, M. Hofmann, *J. Electrochem. Soc.* **2015**, *162*, A384.

[33] D. Landmann, E. Svaluto-Ferro, M. V. F. Heinz, P. Schmutz, C. Battaglia, *Adv. Sci.* **2022**, *9*, 2201019.

[34] T. Javadi, A. Petric, *J. Electrochem. Soc.* **2011**, *158*, A700.

[35] M. C. Bay, M. V. F. Heinz, R. Figi, C. Schreiner, D. Basso, N. Zanon, U. F. Vogt, C. Battaglia, *ACS Appl. Energy Mater.* **2019**, *2*, 687.

[36] R. W. Berg, H. A. Hjuler, N. J. Bjerrum, *J. Chem. Eng. Data* **1983**, *28*, 251.